ZR | Zoological Research

**Article**                                                    **Open Access**

# Overexpression of wild-type HRAS drives non-alcoholic steatohepatitis to hepatocellular carcinoma in mice

Chen Ling[1,2,#], Su-Su Liu[2,#], Yu-Ya Wang[2,#], Gui-Tao Huo[3], Yan-Wei Yang[3], Nan Xu[4], Hong Wang[5], Yong Wu[2], Yu-Fa Miao[3], Rui Fu[5], Yu-Wei Zhao[1,*], Chang-Fa Fan[2,*]

[1] *College of Life Sciences, Northwest University, Provincial Key Laboratory of Biotechnology of Shaanxi Province, Xi'an, Shaanxi 710069, China*

[2] *Division of Animal Model Research, Institute for Laboratory Animal Resources, National Institutes for Food and Drug Control (NIFDC), Beijing 102629, China*

[3] *National Center for Safety Evaluation of Drugs, National Institutes for Food and Drug Control (NIFDC), Beijing 100176, China*

[4] *Division of HIV/AIDS and Sexually Transmitted Virus Vaccines, Institute for Biological Products Control, National Institutes for Food and Drug Control (NIFDC), Beijing 102629, China*

[5] *Division of Laboratory Animal Monitoring, Institute for Laboratory Animal Resources, National Institutes for Food and Drug Control (NIFDC), Beijing 102629, China*

## ABSTRACT

Hepatocellular carcinoma (HCC), a prevalent solid carcinoma of significant concern, is an aggressive and often fatal disease with increasing global incidence rates and poor therapeutic outcomes. The etiology and pathological progression of non-alcoholic steatohepatitis (NASH)-related HCC is multifactorial and multistage. However, no single animal model can accurately mimic the full NASH-related HCC pathological progression, posing considerable challenges to transition and mechanistic studies. Herein, a novel conditional inducible wild-type human *HRAS* overexpressed mouse model (HRAS-HCC) was established, demonstrating 100% morbidity and mortality within approximately one month under normal dietary and lifestyle conditions. Advanced symptoms of HCC such as ascites, thrombus, internal hemorrhage, jaundice, and lung metastasis were successfully replicated in mice. In-depth pathological features of NASH- related HCC were demonstrated by pathological staining, biochemical analyses, and typical marker gene detections. Combined murine anti-PD-1 and sorafenib treatment effectively prolonged mouse survival, further confirming the accuracy and reliability of the model. Based on protein-protein interaction (PPI) network and RNA sequencing analyses, we speculated that overexpression of HRAS may initiate the THBS1-COL4A3 axis to induce NASH with severe fibrosis, with subsequent progression to HCC.

Collectively, our study successfully duplicated natural sequential progression in a single murine model over a very short period, providing an accurate and reliable preclinical tool for therapeutic evaluations targeting the NASH to HCC continuum.

**Keywords:** HRAS; THBS1; HCC driver factor; NASH; Fibrosis; Cirrhosis; HCC; Treatment evaluation

## INTRODUCTION

Cancers, particularly solid carcinomas, exhibit complex and highly heterogeneous etiologies, occurrences, and developmental trajectories, primarily influenced by driver gene mutations/expression (Karlsson et al., 2023; Pan et al., 2023), immune/tumor microenvironment (Donne & Lujambio, 2023), epigenetic alterations (Rahme et al., 2023), and environmental factors (Fujiwara et al., 2018). Hepatocellular carcinoma (HCC) presents as a highly aggressive and often fatal disease with escalating global incidence rates and poor therapeutic outcomes (Orci et al., 2022). Non-alcoholic fatty liver disease (NAFLD) is the second leading cause of chronic liver disease, after viral hepatitis, affecting up to 25% of the global population (Liu et al., 2022). Approximately 20% of NAFLD patients may progress to non-alcoholic steatohepatitis (NASH) (Sheka et al., 2020). Fatty liver is pathogenetically linked to liver fibrosis and cirrhosis development (Thaler, 1962), with cirrhosis representing the highest risk factor for HCC (Mcglynn et al., 2021). Although conclusive evidence remains elusive, the hypothesis that NAFLD/NASH progresses to fibrosis/cirrhosis, eventually leading to HCC, has gained

support in recent years (Anstee et al., 2019; Eslam et al., 2020; Powell et al., 2021), supported by a previous study monitoring 42 NASH patients for up to 21 years (Powell et al., 1990). Given the multiple pathological progressions associated with HCC, adopting a more holistic approach (de la Vega, 2023) rather than singularly focusing on NASH, fibrosis, or cirrhosis progression is imperative. Animal models that accurately mimic the full spectrum of disease progression are critical elements in addressing these complex issues related to HCC.

Over the past several decades, induction of NASH and HCC in murine models has been achieved through various approaches, including genetic manipulation (Suzuki et al., 2022), diet induction (Tsuchida et al., 2018; Yang et al., 2012), carcinogen exposure (Connor et al., 2018; Guo et al., 2023), and a combination of diet and carcinogens, such as diethylnitrosamine (DEN) (de la Rosa et al., 2021). Notably, around 60% of liver-specific augmenter of liver regeneration knockout (ALR-KO) mice develop HCC within one year of birth (Gandhi et al., 2015). Spontaneous hepatocarcinogenesis in transgenic HRAS$^{G12V}$ mice typically manifests between 8- and 13-months post-birth (Kim et al., 2021). Moreover, approximately 50% of C57BL/6 mice subjected to the American lifestyle-induced obesity syndrome (ALIOS) diet for 12 months and maintained under a sedentary lifestyle subsequently develop NASH, fibrosis/cirrhosis, and HCC (Dowman et al., 2014). In summary, existing models are constrained by prolonged induction periods, atypical clinical features, and low rats of HCC induction (Wu, 2016). Consequently, the development of reliable and sophisticated animal models is imperative for elucidating the mechanisms underlying NASH-related HCC occurrence and metastasis and facilitating the development of effective novel therapeutic strategies.

*RAS*, *P53*, and *PTEN* are prominent carcinogenic factors. "Hot-spot" mutations can lead to Ras retention in the GTP-bound state, resulting in the direct activation of several downstream signaling pathways, including the MAPK and PI3K pathways, and contributing to the progression of various human cancers (Moore et al., 2022), such as pancreatic, lung, colon, and bladder cancer (Li et al., 2018; Takeuchi et al., 2000). However, the underlying mechanism for liver cancer remains controversial. Some studies suggest that somatic mutations in the *RAS* gene contribute to abnormal pathway activation involving RAS/RAF and PI3K/PTEN (Hou et al., 2014), while others propose that m$^6$A modification promotes wild-type RAS protein overexpression, thereby contributing to tumorigenesis (Alejandro et al., 2022; Pan et al., 2023). The classic RAS protein comprises KRAS, NRAS, and HRAS. Generally, *KRAS* and *NRAS* exhibit higher mutation frequencies compared to *HRAS* across different cancer types (Schubbert et al., 2007). Emerging evidence has implicated the HRAS protein in HRAS-driven tumorigenesis, given the less frequent mutation of the *HRAS* gene in cancers as well as its frequent overexpression in certain tumor types (Pan et al., 2023). Notably, overexpression of wild-type HRAS has been shown to promote cancer cell proliferation and metastasis (Pan et al., 2023). A previous study involving 351 HCC patients revealed an up-regulation of *HRAS* during various stages of hepatocarcinogenesis, associated with an increase in HCC invasion and recurrence (Newell et al., 2009; Tang et al., 1998). To validate the hypothesis that overexpression of wild-type *HRAS* contributes to the development and progression of HCC, we established a novel HCC mouse model by inducing specific overexpression of wild-type *HRAS* in the liver. This model faithfully recapitulated the natural progression from NASH to HCC, achieving a 100% incidence rate within approximately one month. This mouse model can be utilized for therapeutic evaluations and elucidating the mechanisms underlying HRAS-driven NASH-related HCC occurrence.

## MATERIALS AND METHODS

### Mouse model
The C57BL/6 and Cre-ERT2 mice were acquired from the Institute for Laboratory Animal Resources of the National Institutes for Food and Drug Control (NIFDC, China). The double heterozygote CreERT2; HRAS$^{flox/-}$-HCC (HRAS-HCC) mice, harboring a specific 570 bp *HRAS* sequence insertion, were bred at the same facility. Tamoxifen (TAM) served as an inducer to initiate liver-specific *HRAS* gene expression in the HRAS-HCC mouse model, with corn oil utilized as the solvent. The group with TAM-induced HRAS overexpression was referred to as the HRAS$^{TAM}$ group (HRAS-HCC mice, *n*=77), while the control group receiving corn oil only was referred to as the HRAS$^{non-TAM}$ group (*n*=33). All animals were provided with free access to water and diet and maintained on a 12 h light/dark cycle. All animal experiments were approved by the Experimental Animal Committee of the NIFDC (approval number: 2022-B-050; 2021-B-003). All animal experiments strictly adhered to internationally accepted principles for laboratory animal care and use, following both the ARRIVE and American Veterinary Medical Association (AVMA) guidelines. A total of 126 mice were included in this study without any exclusions within each experimental group.

### Clinical database retrieval
The cBioPortal for Cancer Genomics database (https://www.cbioportal.org), the Cancer Genome Atlas (TCGA) database, the Gene Expression Omnibus (GEO) (GSE20140), and the Kaplan-Meier (KM) Plotter databases were utilized in this study to investigate HRAS expression in clinical HCC patients. The search criteria included all risk factors, excluding alcohol consumption and hepatitis virus infection.

### HRAS-HCC mouse model generation
A human *HRAS* gene fragment using the loxP strategy was inserted into the Rosa 26 allele of C57BL/6 mice, as described in previous study (Feil et al., 2009). HRAS$^{flox/flox}$ mice were bred with Cre-ERT2 mice to obtain double heterozygote mice, which were then subjected to an intraperitoneal injection of 2 mg of TAM (Sigma, USA) per mouse, as per the provided instructions. Intragroup control mice received corn oil at the same age. The mice were sacrificed at indicated time points, and liver tissues were collected and analyzed. A decrease in body weight exceeding 20% was considered indicative of mortality based on the percentage change curve of body weight.

### Genotyping and mutation detection
Genomic DNA from the tail from the offspring was isolated and then subjected to polymerase chain reaction (PCR) amplification. The genotype identification fragment in HRAS-HCC mice comprised four bands, measuring 370 bp, 469 bp, 481 bp, and 385 bp. The base sequences of the inserted

human *HRAS* gene were determined using sequencing (Sangon Biotech, China).

## Reverse transcription-quantitative real-time polymerase chain reaction (RT-qPCR)

To evaluate gene expression levels by RT-qPCR, total RNA was extracted from mouse tissues using RNAisoPlus (Takara, Japan). The RNA concentration was measured using a NanoDrop spectrophotometer. Subsequently, cDNA was synthesized using a PrimeScript™ RT Reagent Kit with gDNA Eraser Kit (Takara, Japan). Real-time PCR was conducted using a Roche quantitative PCR instrument with TB Green® Premix Ex Taq™ (Takara, Japan). GAPDH served as the endogenous control, and each sample was analyzed in triplicate (*n*=3). Further details on the primers used are provided in Supplementary Table S1.

## Protein extraction and western blot analysis

For total protein extraction, tissues were lysed in RIPA buffer containing protease and phosphatase inhibitors. The protein concentration in tissues of both the HRAS^TAM and HRAS^Non-TAM groups was determined using a BCA Protein Assay Kit (Sangon, China). Protein solutions were boiled in 5×loading buffer (ThermoFisher Scientific, USA) at 98°C for 10 min and subsequently resolved by sodium dodecyl-sulfate polyacrylamide gel electrophoresis (SDS-PAGE). All primary antibodies, including HRAS-specific polyclonal antibody (1:1 000, Proteintech, USA) and GAPDH antibody (1:10 000, Abcam, UK), were diluted in 3% BSA (Solarbio, China). Primary antibodies were detected by goat anti-rabbit immunoglobulin G (IgG)-horseradish peroxidase (HRP)-conjugated secondary antibody (1:10 000, Abcam, UK). Chemiluminescence images were captured using a glue applicator (Tanon, China) and gray values were analyzed using ImageJ (https://imagej.net/). Each sample was analyzed in triplicate (*n*=2).

## Magnetic resonance imaging

Hepatomegaly and organ position were assessed using time-domain Echo magnetic resonance imaging (MRI) by the Institute of Laboratory Animals Science, Chinese Academy of Medical Sciences and Peking Union Medical College (CAMS & PUMC).

## Biochemical index detection

Blood samples were obtained from the tail vein of mice following a 4 h fasting period, with serum subsequently separated through centrifugation. Biochemical indices were analyzed using an automatic blood and biochemistry analysis instrument (OLYMPUS AU400, Japan). The study groups consisted of HRAS^TAM (*n*=8), HRAS^non-TAM (*n*=4), and wild-type (*n*=4) mice.

## Hematoxylin and eosin (H&E) staining

The liver tissues from the HRAS^TAM (*n*=30) and HRAS^non-TAM mice (*n*=28) were fixed in formalin (Solarbio, China), embedded in paraffin, and transferred to 70% ethanol (Sinopharm Chemical Reagent, China). Biopsy material from individual liver lobes was placed in processing cassettes, dehydrated through a serial alcohol gradient, and embedded in paraffin wax blocks. Before immunostaining, 5-µm-thick liver tissue sections were dewaxed in xylene (Sinopharm Chemical Reagent, China), rehydrated through decreasing concentrations of ethanol, and washed in phosphate-buffered saline (PBS, Solarbio, China). The sections were then stained

with H&E (Leagene, China), scanned using a NanoZoomer scanner (HAMAMATSU, C13210-01, Japan), and previewed using NanoZoomer Digital Pathology software (NDP Viewer, Japan).

## Immunohistochemical (IHC) analysis

The most representative mice from the HRAS^TAM and HRAS^non-TAM groups were selected each week (at least two mice per group) to detect marker expression. For IHC analysis, liver tissue paraffin sections were dewaxed using xylene and a serial alcohol gradient, followed by incubation in 3% $H_2O_2$ for 15 min and boiling with citrate buffer (pH 6.0) for antigen retrieval. The sections were then blocked with fetal bovine serum (FBS), with the following primary antibodies applied for overnight incubation at 4°C: HRAS-specific polyclonal antibody (1:100, Proteintech, USA), AFP polyclonal antibody (1:100, Proteintech, USA), anti-thrombospondin-1/TSP1 antibody (1:500, Sino-Technology, China), anti-collagen IV rabbit polyclonal antibody (1:500, Sino-Technology, China), and cytokeratin 18 monoclonal antibody (1:200, Proteintech, USA). After washing with PBS, the sections were incubated with secondary antibodies for 1 h at 37°C, then sealed with glycerin (Solarbio, China) following 3,3'-diaminobenzidine (DAB) coloration (ZSGB-BIO, China). The sections were then scanned using a NanoZoomer scanner (HAMAMATSU, C13210-01, Japan) and previewed using NDP Viewer (Japan). The IHC results were analyzed with HALO software (USA). The liver sections used in IHC were from the same mice as those used in H&E staining. The percentage of positive area in IHC was analyzed using ImageJ (https://imagej.net/).

## Immunofluorescence (IF) analysis

For immunofluorescence analysis, liver tissue paraffin sections were dewaxed using xylene and a serial alcohol gradient, followed by incubation in 3% $H_2O_2$ for 15 min and boiling with citrate buffer (pH 6.0) for antigen retrieval. The sections were subsequently blocked with FBS, with the following primary antibody applied for overnight incubation at 4°C: HRAS-specific polyclonal antibody (1:100, Proteintech, USA). After washing three times in PBS, the sections were incubated with fluorescence secondary antibodies (ThermoFisher Scientific, USA) for 1 h at 37°C. Finally, after washing with PBS, the tissues were mounted with sealing agent containing 4',6-diamidino-2-phenylindole (DAPI, ThermoFisher Scientific, USA), then photographed using a laser confocal microscope (Zeiss LSM900 with Airyscan2, Germany) and analyzed using Image 5.czi-ZEN 3.6 software (Zeiss, Germany).

## Oil Red O staining

Mouse liver samples (*n*=2) were fixed in 4% paraformaldehyde (Solarbio, China) for paraffin embedding or frozen sectioning (−15°C). Subsequently, 60% isopropanol immersion was performed on 8-µm-thick sections, followed by staining with Oil Red O dye solution (Leagene, China) for 10 min. After washing with 60% isopropanol, the sections were counterstained with hematoxylin (Leagene, China). Histopathological examination of the aorta and liver was performed using an Olympus BH2 microscope and results were analyzed using HALO software (USA).

## Sirius Red staining

Liver sections (*n*=3) were cut (5 µm thick) and dewaxed conventionally. The sections were then stained with

hematoxylin staining solution for 10 min and washed using distilled water. Following the application of Sirius Red staining solution (Leagene, China) for 15 min, the sections were rinsed slightly with running water. Dehydration was achieved by a series of ethanol solutions, starting from 75% ethanol, followed by transparentizing with xylene and sealing with glycerin. The sections were scanned using a NanoZoomer scanner (HAMAMATSU, C13210-01, Japan) and previewed using NDP Viewer (Japan). The polarized light photos were captured using an Olympus BMP-107 series microscope (Japan).

## Masson staining

Liver slices were placed into Bouin's fluid and left at room temperature overnight, then washed with running water until the yellow color disappeared. Celestin blue B staining solution (Leagene, China) was applied for 2 min, followed by staining with spring red fuchsin (Leagene, China) solution after acid ethanol differentiation. The slices were then treated with phosphomolybdic acid solution (Leagene, China) and stained with aniline blue (Leagene, China). After weak acid treatment, they were dehydrated and made transparent before sealing. The sections were the scanned using a NanoZoomer scanner (HAMAMATSU, C13210-01, Japan) and previewed using NDP Viewer. This process was repeated with at least three different mouse liver tissue samples per group.

## Copper salt staining

Liver tissue sections ($n$=2) were cut (5 μm thick) and conventionally dewaxed. The sections, along with positive control sections, were soaked in distilled water, then stained with dithiooxamide staining solution (Leagene, China) in a 37°C water bath for 24 h. After rinsing with 70% ethanol and washing slighting with distilled water, the sections were stained with nuclear fast red solution (Leagene, China) for 1 min, then conventionally dehydrated, transparentized, and sealed with glycerin. The sections were scanned using a NanoZoomer scanner (HAMAMATSU, C13210-01, Japan) and previewed using NDP Viewer.

## Selection principle for pathological staining

To illustrate the co-occurrence of NASH, fibrosis, and cirrhosis with HCC and typical symptoms, we systematically sampled tissues for continuous slicing at fixed intervals and for staining, including H&E, IHC, Sirius red, Masson, and Copper salt staining (mouse number: 1 W 011, 2 W 01, 3 W 09, 4 W 13).

## Clinical treatment of HCC mice

Mice in the TAM group were subjected to different regimens, with four groups established: sorafenib group (SO, Selleckchem, USA), anti-mouse PD-1 group (PD-1, BioCell, USA), sorafenib combined with PD-1 (P&S) group, and solvent control group (ME). The SO group was treated with 30 mg/kg sorafenib dissolved in 1% CMC-Na (Sigma, USA), PEG400 (Sangon Biotech, China), and $H_2O$ via gastric irrigation. The PD-1 group was treated with 5 mg/kg of anti-mouse PD-1 via intragastric administration. The P&S-1 group was treated with sorafenib and anti-mouse PD-1 twice a week for two consecutive weeks, while the P&S-2 group received additional doses of anti-mouse PD-1 at week 4 based on the treatment of P&S-1. The ME group was treated with the same dose of CMC-Na, PEG400, and DMSO (Sigma, USA). Survival analysis was conducted based on the median survival time.

## RNA sequencing (RNA-seq)

RNA-seq was performed on the HRAS[TAM] ($n$=5) and HRAS[non-TAM] ($n$=4) mice at 1–2 W. The library fragments were purified using the AMPure XP system (Beckman Coulter, Beverly, USA) and sequenced using the Illumina NovaSeq 6000 platform (Illumina, USA). The reference genome index and paired-end clean reads were aligned using HISAT2 (v.2.0.5). Differential expression analysis of the two groups was performed using the DESeq2 R package (v.1.20.0). $P$-values were adjusted using the Benjamini & Hochberg method, with $P$-adjust≤0.05 and $|\log_2(\text{fold-change})|$≥1.2 set as the thresholds for significantly differentially expressed genes (DEGs). The ClusterProfiler R package (v.3.8.1) was employed to identify significantly enriched Kyoto Encyclopedia of Genes and Genomes (KEGG) pathways among the DEGs, with a corrected $P$-value<0.05 considered significant. Shared DEGs were imported into the STRING (v.12.0, https://www.string-db.org/) web tool to map the protein-protein interaction (PPI) network. The MCODE plugin in Cytoscape (http://www.cytoscape.org/) was used to analyze the PPI network for functional modules of DEGs.

## Analysis of pathological and special staining

Digital whole-slide multispectral images were scanned using a NanoZoomer scanner (HAMAMATSU, C13210-01, Japan). Quantitative image analysis was performed using HALO software (v.3.0.311.405, Indica Labs, USA) on at least one liver longitudinal section from each animal. For Oil red O staining, the area quantification brightfield module was used to detect the Oil red O-positive area and the proportion (%) of the positive area to the total tissue area. The object analysis BF module was used to identify lipid droplets in the Oil red O-positive expression region, as well as the particle size range (μm) and lipid droplet density (lipid droplet number/mm²) of the lipid droplets.

## Statistical analysis

All statistical analyses were performed using Prism v.8.0 (GraphPad, USA). Statistical significance between two groups was calculated using unpaired student $t$-test. Data involving more than two groups were compared using a one-way analysis of variance (ANOVA), followed by Tukey's multiple comparison tests (to compare means of each column with means of every other column). *: $P$<0.05 was considered statistically significant. Survival analysis was determined based on the median survival time. Most experiments were carried out at least three times, and the findings of all key experiments were reliably reproduced.

## RESULTS

### Establishment of HRAS-HCC mouse model with human *HRAS* gene inducible overexpression in the liver

To explore the role of the *HRAS* gene in HCC development, genomic data from the TCGA, GEO (GSE20140), and KM Plotter databases were retrieved and analyzed. Results revealed that the mutation frequency of HRAS in HCC patients was notably low, constituting only 0.8% (Figure 1A), but HRAS expression was significantly up-regulated in these patients (Figure 1B; Supplementary Figure S1A and Table S2). Survival analysis based on data from the TCGA, GEO (GSE20140), and KM Plotter databases indicated a strong correlation between HRAS up-regulation and poor prognosis (Figure 1C, D; Supplementary Figure S1B–D), particularly
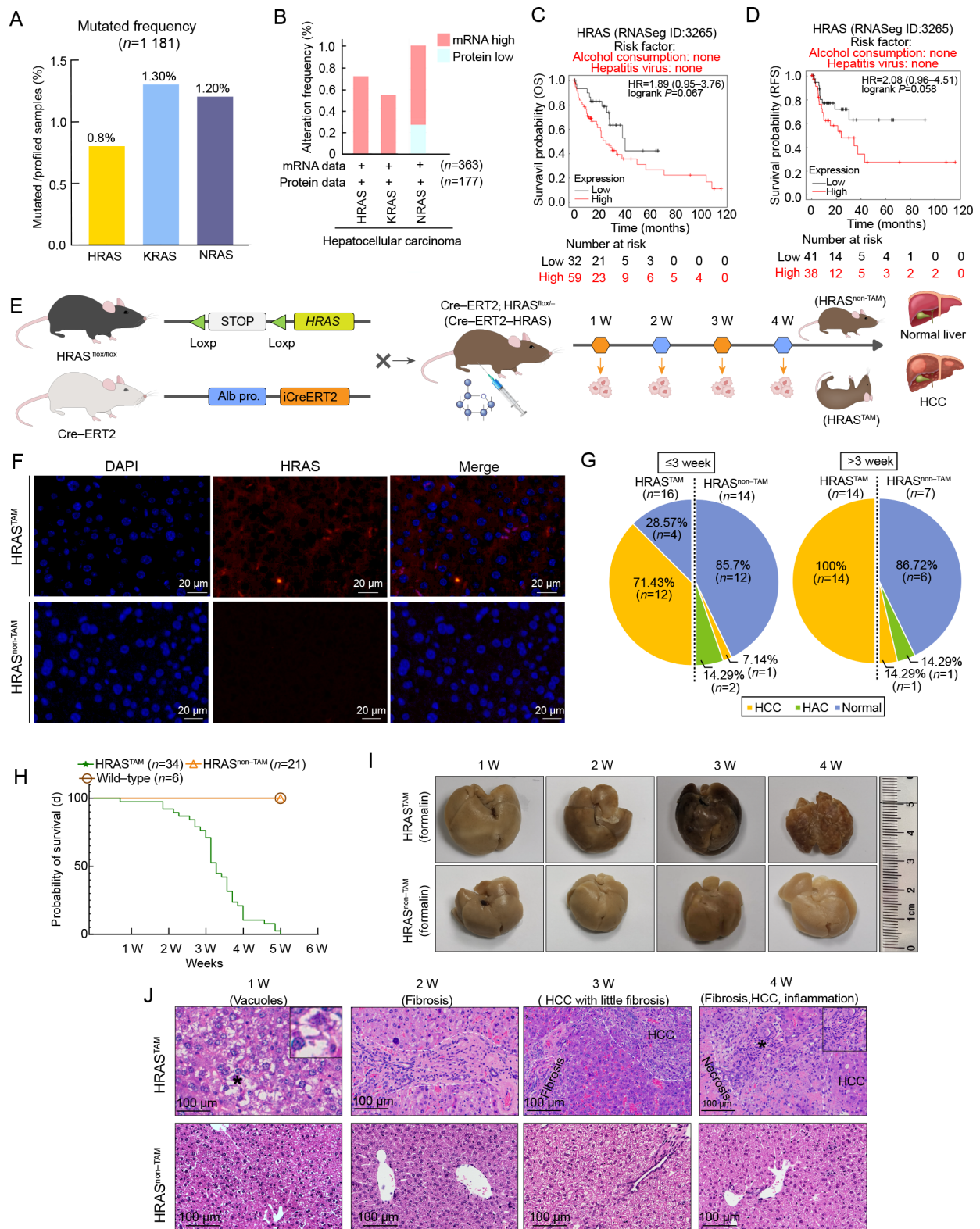
**Figure 1  Generation of a knock-in mouse model expressing the human *HRAS* gene in the liver**

A: Mutated frequency of *RAS* family in HCC patients from the cBioPortal for Cancer Genomics database. B: mRNA and protein expression levels of HRAS, KRAS, and NRAS in HCC patients from the TCGA database. C, D: Survival of HRAS-expressing HCC patients from KM-plot.com. Cohort in C and D did not include patients with alcoholic fatty liver disease or hepatitis virus infections. E: Generation of HRAS[flox/-];Cre-ERT2 mouse model. Intraperitoneal injection of TAM induced *HRAS* overexpression in mice, with corn oil used as a solvent. Tissues were collected at different weeks after *HRAS* overexpression. F: Immunofluorescence of HRAS (red) and DAPI (blue) in livers of HRAS[TAM] mice was stronger than that in HRAS[non-TAM] mice in week 1 (*n*=3). Scale bar: 20 μm. G: Morbidity and mortality of HCC in mice at weeks 3 to 4 were 100%. H: Survival of HRAS[TAM] (*n*=34), HRAS[non-TAM] (*n*=21), and wild-type mice (*n*=6). I: Formalin-treated liver morphology in HRAS[TAM] and HRAS[non-TAM] mice at weeks 1 to 4. J: Pathological analysis of HCC progression in the livers of HRAS[TAM] and HRAS[non-TAM] mice based on H&E staining at weeks 1 to 4. White dashed line represents outline of diseased area, like fibrosis, necrosis, and HCC. Black asterisks mark magnified areas. Scale bar: 100 μm.

among NASH-associated HCC patients without alcohol consumption or hepatitis virus infection (Figure 1C, D). Collectively, these findings suggest that non-mutated HRAS up-regulation may be associated with the occurrence of NASH-associated HCC.

HRAS up-regulation was associated with both HCC occurrence and poor prognosis (Figure 1A–D; Supplementary Figure S1A–D). In accordance with on our previous study, wherein systemic overexpression of *HRAS* resulted in embryonic lethality before E15 (Liu et al., 2018), we aimed to establish a liver-specific inducible *HRAS* overexpressed mouse model using embryonic cell targeting technology. Notably, the full cDNA of *HRAS* was inserted behind the CAG promoter and spaced using a loxP-stop element, resulting in the generation of genetically modified HRAS[flox/flox] mice, which were subsequently crossed with TAM-inducible Cre-ERT2 mice to produce Cre-ERT2-HRAS mice. Thus, based on an integrated and optimized TAM induction approach (Lizen et al., 2015), the liver-specific overexpressed wild-type *HRAS*-HCC mouse model was established, as detailed in Figure 1E and Supplementary Figure S1E. The *HRAS* transgene remained in a non-mutated state in mice, as confirmed by sequencing (Supplementary Figure S1F). Importantly, TAM-inducible *HRAS* overexpression was confined solely to the liver by day 7 (Supplementary Figure S1G), and *HRAS* expression in the TAM-treated mice (HRAS[TAM]) increased in a time-dependent manner (Supplementary Figure S1H–J), consistent with previous research (Reinert et al., 2012). Notably, *HRAS* expression increased at week 1 (Figure 1F) and increased significantly from weeks 3 to 4 (Supplementary Figure S1H). These findings confirm the successful establishment of an HCC mouse model by inducible liver-specific overexpression of the human *HRAS* gene.

## HRAS-HCC mouse model faithfully mimics clinical features of HCC

To corroborate clinical observations (Figure 1G–I; Supplementary Figure S2A–D and Table S3), we assessed whether *HRAS* overexpression in the mouse liver led to severe HCC. Our findings indicated that mice developed HCC and succumbed to it within 3 weeks post-*HRAS* overexpression. Therefore, we evaluated the incidence of HCC by histological examination of H&E-stained liver sections at two time points. At 3 weeks, the incidence of HCC increased from 71.43% to 100% (Figure 1G). Conversely, the incidence of HCC remained low in the TAM-untreated mice (HRAS[non-TAM]). Continuous *HRAS* expression resulted in 100% mortality (Figure 1H) and notable body weight loss (Supplementary Figure S2A), while also promoting the development of typical clinical symptoms, such as hepatomegaly, liver calcification, jaundice, and cachexia (Supplementary Figure S2B). Furthermore, manifestations of HCC symptoms, such as ascites, internal bleeding, hypersplenism, and dyspnea, were observed in the HRAS[TAM] group. Jaundice was also observed in the skin, paws, and peritoneum (Supplementary Figure S2C), which is hard to be observed in other rodent models of HCC. *In vivo* MRI analyses showed hepatomegaly in all HRAS[TAM] mice (Supplementary Figure S2D), consistent with previous findings (Younossi et al., 2018b). These results demonstrate that this mouse model faithfully recapitulates both the clinical and pathological characteristics of HCC, displaying a rapid disease onset under normal lifestyle and dietary conditions.

*HRAS* overexpression resulted in a time-independent increase in liver weight and the liver/body weight ratio (Supplementary Figure S2E, F), with a marginal but significant time-independent decrease in alkaline phosphatase (ALP) concentrations (Supplementary Figure S2G). The decline in ALP levels indicated the presence of kidney injury, specifically renal hemorrhage (Supplementary Figure S2B), consistent with previous research (Su et al., 2022). Conversely, alanine aminotransferase (ALT) levels appeared unaffected (Supplementary Figure S2H), suggesting that this HCC mouse model may exhibit unique pathological characteristics compared to others (De Martin et al., 2020; Jeng et al., 2023).

## HRAS-HCC mouse model faithfully mimics pathological features of HCC

To confirm pathological features, H&E-stained liver sections from HRAS[TAM] mice from weeks 1 to 4 were analyzed (Figure 1J; Supplementary Figure S2I). At week 1, typical NASH-associated pathological features were observed, including increased basophilia and vacuolated cells around hepatic veins, along with vacuolation at tissue margins. With NASH progression, vacuolated lesions gradually disappeared, transitioning to severe fibrotic and necrotic lesions, ultimately leading to HCC development (Figure 1J). Specific pathological features indicative of HCC, such as fibrosis and necrosis (marked by white dashed lines), were observed at different time points (Figure 1J). At week 4, the formalin-fixed liver tissues exhibited a friable and dehydrated appearance with a rough surface and pseudo-lobules suggestive of cirrhosis (Figure 1J; Supplementary Figure S3A). In addition, *HRAS* overexpression induced liver tissue calcification and necrosis/fibrosis (white spots), indicating the presence of space-occupying lesions (Supplementary Figure S3B–D). These findings demonstrate that the HRAS-HCC mouse model faithfully recapitulates HCC manifestations and accurately replicates progression from NASH to fibrosis, cirrhosis, and ultimately HCC.

All HRAS-HCC mice uniformly developed to HCC within approximately 4 weeks. Our model exhibited typical HCC phenotypic features, including sinusoidal dilatation (Figure 2B, a), severe cytokinesis (inflammatory infiltration; Figure 2Bb), increased cytoplasmic basophilia, transparent droplets (Figure 2Bb), ductular proliferation (Figure 2Bc), thrombi (Figure 2B, d; Supplementary Figure S3Ea–c), hepatocellular hyperplasia (Figure 2Be), and lung metastasis (Figure 2Bf). Notably, cancer was evident even in the early NASH stage (Figure 2Aa), and persisted in the following fibrosis, cirrhosis, and HCC stages (Figure 2Ab–d). This suggests that cancer is the predominant characteristic and may coexist with NASH and fibrosis, consistent with clinical observations (Kern et al., 2019). The expression of the HCC marker gene alpha-fetoprotein (*AFP*) displayed a continuous upward trend (Figure 2C). Additionally, other markers such as *Ki67* were elevated at the NASH stage (Figure 2D), while bile salt export pump gene (*BSEP*, also known as *ABCB11*) expression was lower in the HRAS[TAM] group (Figure 2E), and transthyretin gene (*TTR*) expression was similar between the two groups but tended to be lower in the HCC stage (Figure 2F). These findings are consistent with the down-regulation of *BSEP* and *TTR* in cancer (Wang et al., 2022; Wang et al., 2021). Immunohistochemical staining also revealed strong HRAS and AFP signals in liver tissues from weeks 1 to 3 (Figure 2G, H), which decreased by week 4 (Figure 2G, H), likely due to
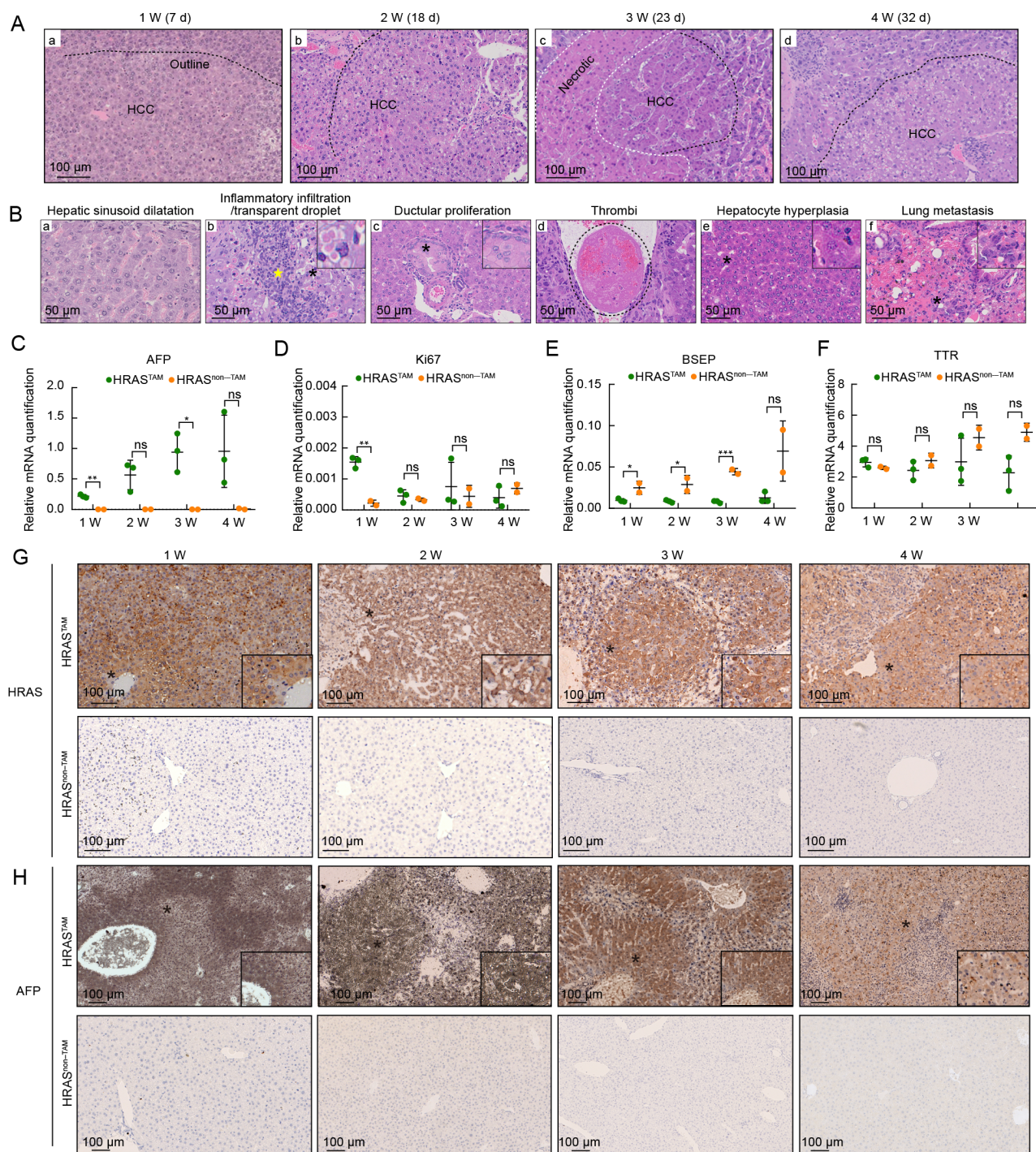
**Figure 2 HRAS-expressing mice exhibit rapid onset of HCC with typical clinical symptoms**

A: Typical histopathological features of HCC by H&E staining. Black dashed line represents the outline of HCC. Scale bar: 100 μm. Some liver tissues were from the same mice in Figure 1J. B: Other typical HCC histopathological features by H&E staining. Black dashed line represents outline of thrombi. Yellow star mark area of inflammatory infiltration. Black asterisks mark magnified areas, respectively. Scale bar: 50 μm. Some liver tissues were from the same mice in Figure 1J. C–F: mRNA expression of *AFP* (B), *Ki67* (C), *BSEP* (D), and *TTR* (E) in HRAS$^{TAM}$ (*n*=3) and HRAS$^{non-TAM}$ (*n*=2) mice. Each sample was repeated three times. Data represent mean±standard deviation (SD). ns: Not significant; *: *P*<0.05; **: *P*<0.01; ***: *P*<0.001; ****: *P*<0.0001. G, H: Immunohistochemical expression of HRAS (G) and AFP (H) in HRAS$^{TAM}$ and HRAS$^{non-TAM}$ mice. Scale bar: 100 μm. Liver tissues were from the same mice in Figure 1J.

increased necrosis in the advanced HCC stage.

**NASH is the initial stage of HCC**

As most HRAS$^{TAM}$ mice exhibited liver lesions at week 1, their serum was examined. Results demonstrated that *HRAS* overexpression led to increased serum turbidity over time (Figure 3A; red boxes), resembling observations in patients

with hyperlipidemia (Behera et al., 2020; Chaurasiya et al., 2013; Dildar & Shamsi, 2020). Chylemia was initially detected in week 1 and persisted until week 2 but became undetectable by weeks 3 and 4. Subsequent examinations revealed elevated cholesterol (CHO) and triglyceride (TG) concentrations in HRAS$^{TAM}$ mice. While CHO levels remained
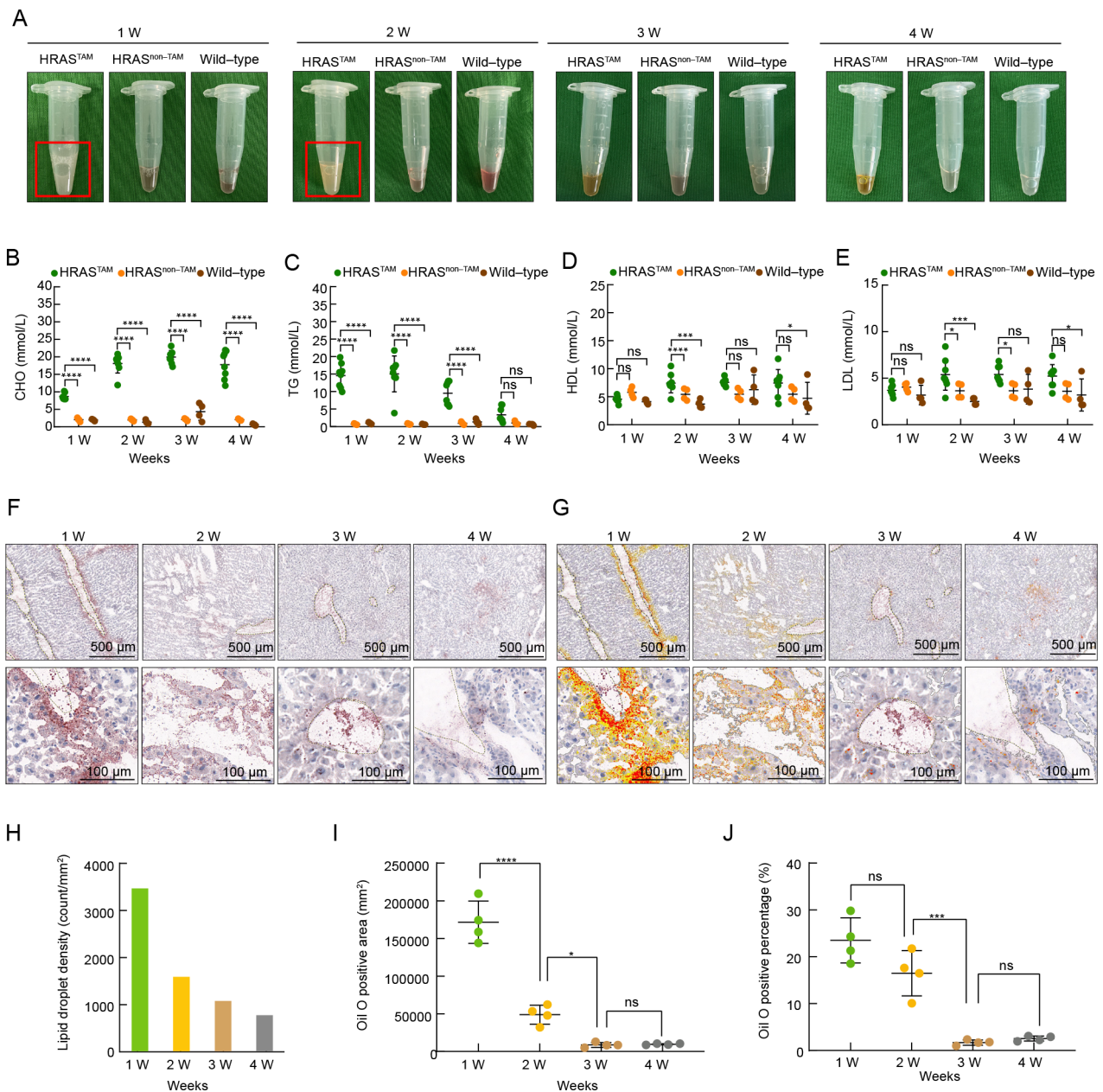
**Figure 3 Features of the initial stage NASH in HCC mice**

A: Changes in serum turbidity in HRAS^TAM^, HRAS^non-TAM^, and wild-type mice. White chylous blood (red boxes) occurred at weeks 1 to 2 and gradually disappeared with disease development. B–E: Concentrations of biochemical markers CHO (B), TG (C), HDL-C (D), and LDL-C (E) in serum of HRAS^TAM^, HRAS^non-TAM^, and wild-type mice. F, G: Lipid droplets in liver tissue of HRAS^TAM^ mice (Oil red O staining). Scale bars: 500 μm and 100 μm. H–J: Lipid droplet density, positive area, and percentage of positively-stained areas in liver tissue of HRAS^TAM^ mice. Data represent mean±SD. ns: Not significant; *: $P<0.05$; **: $P<0.01$; ***: $P<0.001$; ****: $P<0.0001$.

elevated throughout disease progression, TG levels returned to baseline (Figure 3B, C). No significant differences were found in low-density lipoprotein cholesterol (LDL-C) and high-density lipoprotein cholesterol (HDL-C) levels between the groups (Figure 3D, E). Additionally, Oil red O staining revealed prominent lipid droplet deposition around hepatic arteries and veins at week 1, which subsequently decreased (Figure 3F). In contrast, control mice demonstrated minimal to no lipid droplet deposition (Supplementary Figure S3F). Quantitative analysis of lipidosis using HALO (Figure 3G) indicated that lipid droplet density, total stained area, and percentage of positively stained areas were highest at week 1 and tended to decrease over time (Figure 3H–J). Furthermore, large lipid droplet (defined as diameter>1 μm) deposition predominantly

occurred in the NASH stage (Supplementary Figure S3G), consistent with previous research (Schott et al., 2019). These findings suggest that during the initial phases of HRAS^TAM^ mouse model development, features akin to steatosis are observed, indicating that NASH may be a trigger for HCC

### Severe fibrosis/cirrhosis is the second stage of HCC

Given the crucial role of fibrosis/cirrhosis in HCC progression, we conducted further investigations to determine whether HCC mice could accurately mimic the development of fibrosis and cirrhosis. Fibrosis, a complex response to injury or maladaptive repair processes, can eventually lead to cirrhosis characterized by excessive deposition of collagen and other extracellular matrix (ECM) components in tissues (Alqudah

et al., 2020; Chinese Society of Hepatology, Chinese Medical Association, et al., 2020; Krizhanovsky et al., 2008; Tsuchida et al., 2018; Younossi et al., 2018b). The mRNA expression levels of the fibrosis markers such as collagen type IV Alpha 3 (*COL4A3*), transferrin receptor (*TFRC*) (Unamuno et al., 2021), and the cirrhosis marker keratin 18 (*KRT18*) were higher in the HRAS[TAM] group (Figure 4A–C), with immunohistochemical staining showing a strong COL4A3 signal (Figure 4I; Supplementary Figure S4D). In line with previous research (Blackburn et al., 2016), a notable reduction
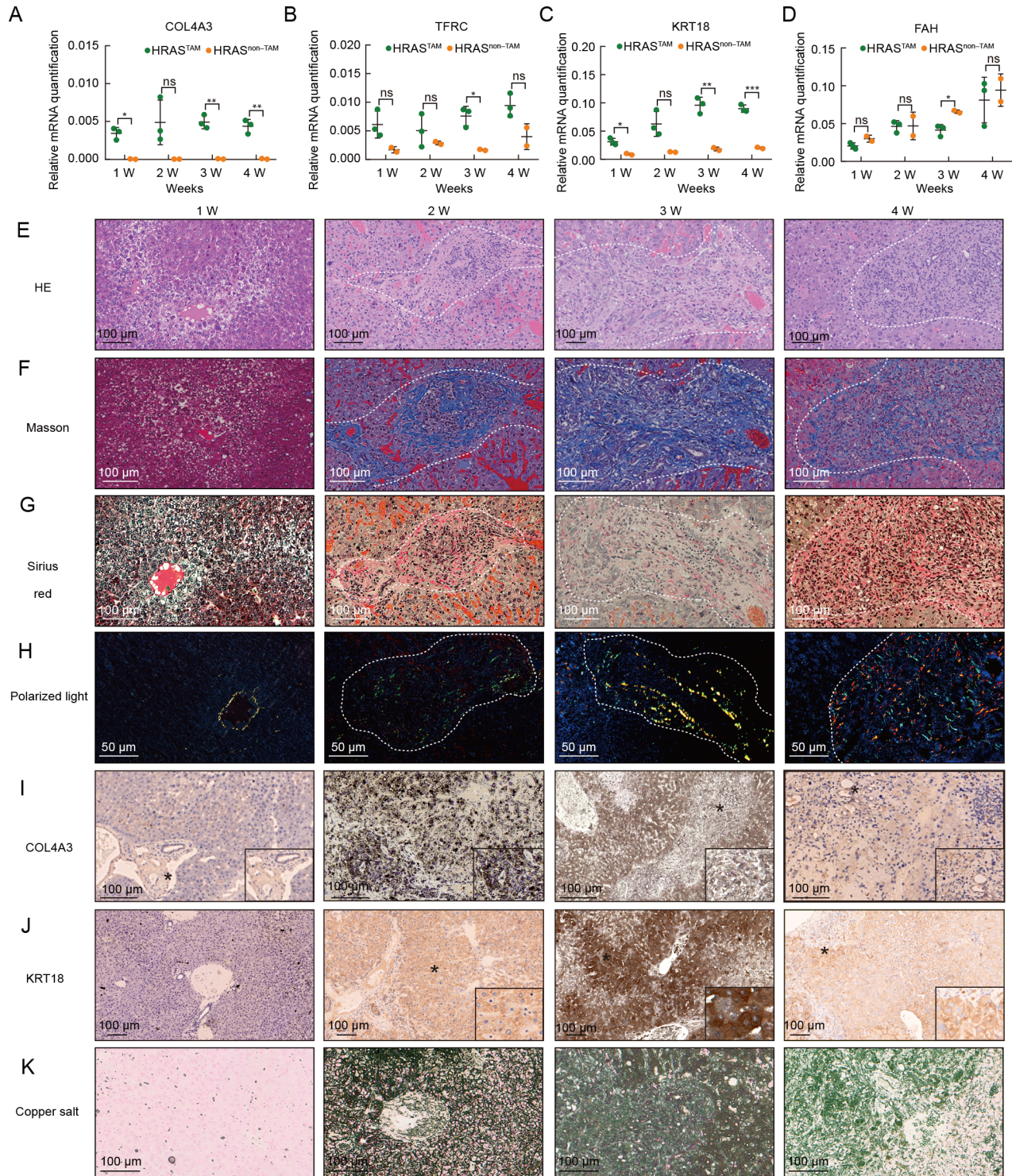


**Figure 4  Characteristics of hepatic fibrosis/cirrhosis stage in HCC mice**

A–D: mRNA expression levels of *COL4A3*, *TFRC*, *KRT18*, and *FAH* in HRAS[TAM] and HRAS[non-TAM] mice. E–G: Histological analysis of livers in HRAS[TAM] mice at weeks 1 to 4 (H&E, Masson, and Sirius red staining). Scale bar: 100 μm. Liver tissues were from the same mice in Figure 1J. H: Polarized light microscopy of livers in HRAS[TAM] mice at weeks 1 to 4 W. Scale bar: 50 μm. Liver tissues were from the same mice in Figure 1J. I, J: Immunohistochemical expression of COL4A3 and KRT18 in livers of HRAS[TAM] mice. Scale bar: 100 μm. Liver tissues were from the same mice in Figure 1J. K: Copper salt staining of livers of HRAS[TAM] mice at weeks 1 to 4. Scale bar: 100 μm. Liver tissues were from the same mice in Figure 1J. Data represent mean±SD. ns: Not significant; *: $P<0.05$; **: $P<0.01$; ***: $P<0.001$; ****: $P<0.0001$.

in *FAH* mRNA levels was observed at 3 weeks (*P*<0.05) in the HRAS-HCC mouse model (Figure 4D), indicating the presence of cirrhosis.

H&E, Sirius red, and Masson staining and polarized light microscopy of serial liver tissue sections showed the presence of fibrosis at week 2 and extensive necrosis at weeks 3 and 4 (Figure 4E–H; Supplementary Figure S4A–C), consistent with earlier studies (Rittié, 2017). Fibrosis initiation was observed in the portal area (Figure 4E–H), advancing to more severe fibrosis and necrosis in the interlobular parenchyma (Figure 4E–H, white dashed lines; Supplementary Figure S4G–I, yellow dashed lines). Furthermore, copper salt staining corroborated the presence of cirrhotic features (Poujois & Woiman, 2018) and extensive necrosis (Young, 2018) in the livers of HRAS-HCC mice at week 2 (Figure 4K; Supplementary Figure S4F), including lobular damage, fibrous bands, and irregular nodules (Figure 4K). Additionally, elevated expression of the cirrhosis marker KRT18 (Figure 4C, J) and the presence of irregular nodules indicated the potential occurrence mechanism of post-necrotic cirrhosis (Figure 4J, K). Collectively, the expression patterns of fibrosis/cirrhosis markers combined with staining of serial sections confirmed that NASH progresses to fibrosis and cirrhosis.

### Combination therapies of anti-mouse PD-1 and sorafenib prolonged HRAS-HCC mouse survival

Therapeutic options for HCC in clinical settings are limited, and prognosis remains unfavorable (Foerster et al., 2022). The efficacy of a novel HCC therapy involving sorafenib (Tang et al., 2020; Yau et al., 2022) and anti-mouse PD-1 (Chuah et al., 2022; Shi et al., 2022) was evaluated in this HRAS-HCC model. Animals were randomly assigned to receive anti-mouse PD-1, sorafenib, or both drugs (P&S) twice a week by intraperitoneal injection (anti-mouse PD-1) or gastric irrigation (sorafenib) starting at week 1 post-TAM induction (Figure 5A). Compared to the solvent control group (ME), the combination therapies marginally reduced the mRNA expression levels of *HRAS* (Figure 5B), *KRT18* (Figure 5F), and *FAH* (Figure 5G), as well as the expression of *COL4A3* (Figure 5D), but had no impact on the expression levels of *AFP* (Figure 5C), *TFRC* (Figure 5E), *Ki67* (Figure 5H), and *ALB* (Figure 5I). Furthermore, treatment had no effect on ALT, ALB, and AST serum levels, liver weight, liver-to-brain ratio, or body weight (Figure 5J–O). Notably, P&S combination therapy prolonged survival by 2 days, while additional supplementary anti-mouse PD-1 (P&S-P) extended survival by 15 days (Figure 5P). These results demonstrate that this HCC murine model faithfully reflects the therapeutic effects of anti-mouse PD-1 and sorafenib, effectively suppressing the elevated expression of markers, *HRAS*, *COL4A3*, *FAH*, and *KRT18*.

### Potential action of HRAS in driving NASH progression to HCC

The complex mechanisms governing the transition from NASH to HCC are not yet fully understood (Wu, 2016). To explore the potential involvement of *HRAS* in driving NASH progression to HCC, liver transcriptome profiles were analyzed by RNA-seq. In total, 2 297 and 2 812 significant DEGs were identified at weeks 1 and 2, respectively, meeting the criteria |log$_2$(fold-change)|≥1.2 and *P*-adjust<0.05 (Figure 6A; Supplementary Tables S4, S5). Additionally, 1 573 DEGs were shared across both time points (Figure 6B; Supplementary Table S6). Based on KEGG analysis, these

DEGs were primarily enriched in lipid metabolism pathways, such as arachidonic acid metabolism, retinol metabolism, and steroid hormone biosynthesis (Figure 6C; Supplementary Table S7), all of which are associated with NAFLD (Zhu et al., 2024). Further analysis revealed the regulatory relationships between *HRAS* and the top 100 up-regulated and down-regulated DEGs through PPI network (Supplementary Figure S5A) and Cytoscape analyses. Notably, thrombospondin 1 (*THBS1*), cyclin dependent kinase inhibitor 2B (*CKN2B*), and erythropoietin (*EPO*) were found to directly interact with *HRAS*. This suggests that *HRAS* overexpression may drive the transition from NASH to HCC via the HRAS-THBS1-COL4A3, HRAS-EPO, and HRAS-CDKN2B-THBS1 axes (Figure 6D; Supplementary Figure S5A). THBS1, an adipokine highly expressed in obesity and insulin-resistant individuals, has been reported as a major activator of TGF-β signaling and implicated in triggering fibrosis (Atanasova et al., 2019; Daniel et al., 2004; Zhang et al., 2015). We hypothesized that THBS1 may be a potential effector of HRAS, with the HRAS-THBS1-COL4A3 axis potentially participating in the progression of NASH to HCC. The elevated mRNA expression of *THBS1* in weeks 2 and 3 confirmed by RT-qPCR and RNA-seq (Figure 6E), as well as the strong immunohistochemical signal of THBS1 consistent with HRAS (Figure 6F) and increased level of COL4A3 (Figure 4A, I), provide partial evidence supporting our hypothesis. In summary, we posited that HRAS overexpression may drive the progression of NASH to HCC via initiation of the THBS1-COL4A3 axis, ultimately leading to HCC. However, further studies are needed.

### DISCUSSION

NASH-related HCC, characterized by its aggressive nature and poor prognosis, is experiencing a concerning increase in global incidence (Febbraio et al., 2019). In addition to its association with obesity and insulin resistance, NASH-related HCC can also manifest in lean individuals under normal lifestyle conditions (Younossi et al., 2018a). Despite lean NAFLD constituting 5%–27% of NAFLD patients (Premkumar & Anand, 2021), the underlying triggers remain elusive, highlighting the complex and multifactorial pathogenesis of NASH-related HCC. Effective treatment strategies are urgently required (Pfister et al., 2021), particularly given the challenges of sorafenib resistance (Huang et al., 2020), lower response rates to anti-PD1 immunotherapy (15%–30%) (Pfister et al., 2021), and limited surgical options due to HCC complications (Chang et al., 2020), contributing to poor long-term survival among NASH-related HCC patients. At present, our understanding of the complex mechanisms involved in NASH-related HCC remains incomplete (Yahoo et al., 2023), largely hampered by the lack of robust experimental models that adequately recapitulate the full disease spectrum (Febbraio et al., 2019). In this study, we established a novel liver-specific human *HRAS* overexpression mouse model (HRAS-HCC), departing from previous strategies involving western lifestyle emulation, lipid metabolism gene manipulation, and carcinogen induction.

Remarkably, this HRAS-HCC mouse model faithfully recapitulated typical clinical and pathological symptoms, with a 100% morbidity rate and all mice succumbing within 5 weeks (Supplementary Figure S2A–H). As such, this model addresses the limitations of existing rodent HCC models, characterized by lower morbidity rates (≤50%), longer modeling cycles (16–50 weeks), and atypical symptomatology
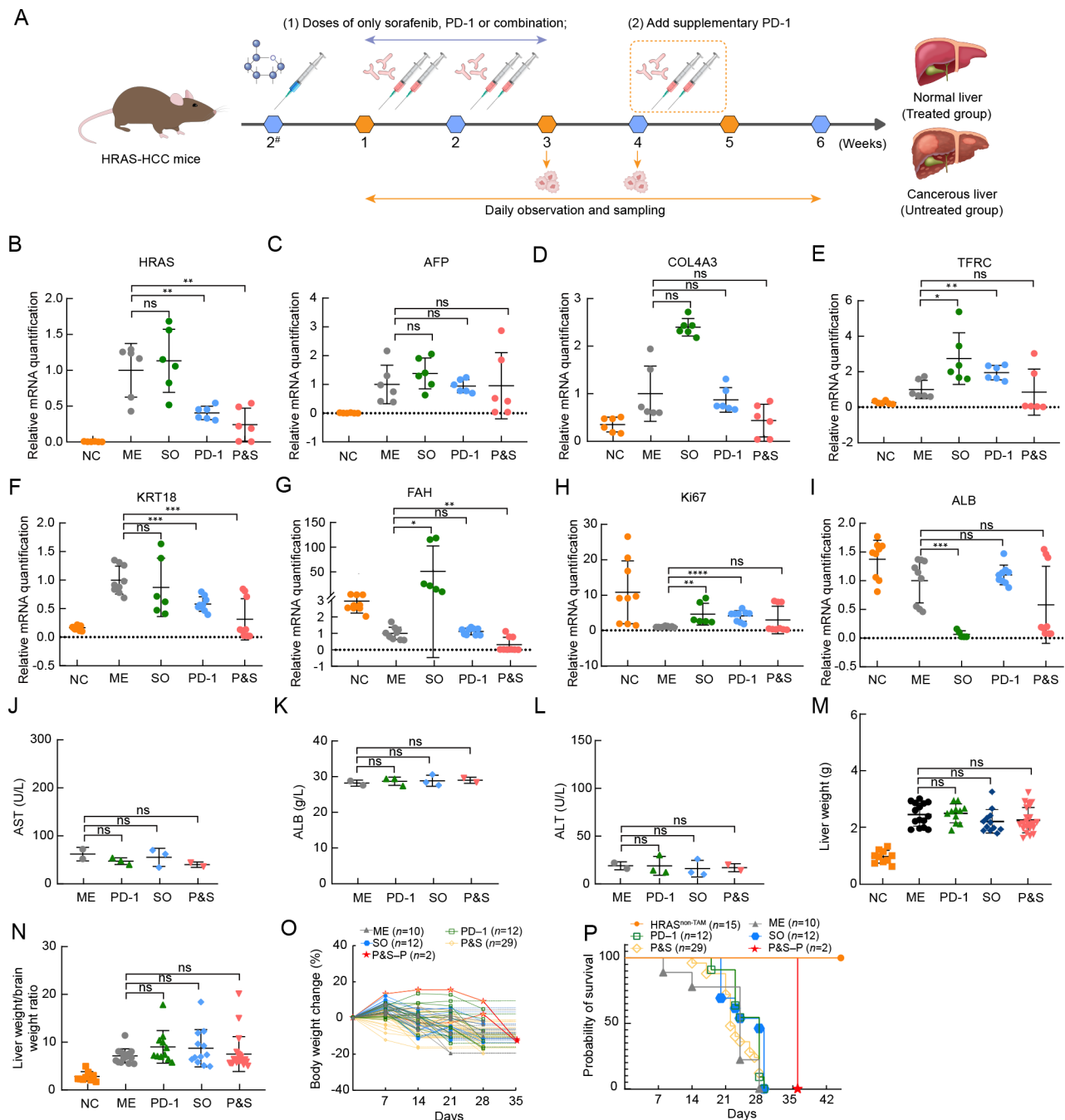
**Figure 5 Combination therapy of anti-mouse PD-1 and sorafenib**

A: Treatment strategy for HCC. B–I: Effects of clinical therapy on mRNA expression of *HRAS* (B), *AFP* (C), *COL4A3* (D), *TFRC* (E), *KRT18* (F), *FAH* (G), *Ki67* (H), and *ALB* (I) in livers of treated mice (*n*=3). J–L: Serum levels of biochemical markers AST (J), ALB (K), and ALT (L) after clinical therapy treatment (*n*=3). Each sample was repeated three times. M, N: Liver weight (M), and liver weight/brain weight ratio (N) after clinical therapy treatment. NC (*n*=10); ME (*n*=15); PD-1 (*n*=11); SO (*n*=12); P&S (*n*=22). O: Body weight after clinical therapy treatment. ME (*n*=10); PD-1 (*n*=12); SO (*n*=12); P&S-1 (*n*=29); P&S-P (*n*=2). Body weight decrease exceeding 20% was defined as death. P: Survival after clinical therapy treatment. Survival was analyzed by median survival time. NC (*n*=10); ME (*n*=10); PD-1 (*n*=12); SO (*n*=12); P&S-1 (*n*=29); P&S-P (*n*=2). Groups are NC: HRAS^non-TAM, ME: CMC-Na, PEG400, and dimethyl sulfoxide (control); SO: sorafenib; PD-1: anti-mouse PD-1; P&S-1: sorafenib combined with anti-mouse PD-1; P&S-P: sorafenib combined with anti-mouse PD-1 and twice supplementary anti-mouse PD-1 in week 4. Data represent mean±SD. ns: Not significant; $^*$: $P<0.05$; $^{**}$: $P<0.01$; $^{***}$: $P<0.001$; $^{****}$: $P<0.0001$.

(Dowman et al., 2014; Fujii et al., 2013; Kawai et al., 2012). Notably, the HRAS-HCC mouse model revealed novel features, such as ascites, thrombus, hypersplenism, internal hemorrhage, jaundice, and HCC with lung metastasis, marking the first description of such traits in a mouse model of HCC (Figure 2; Supplementary Figure S2). These features align with decompensated cirrhosis manifestations associated with a higher risk of mortality (1-year survival of approximately 50%) in clinical settings (Garcia-Tsao et al., 2009; Mu et al., 2020; Mudumbi et al., 2018). The observed decrease in BSEP (Figure 2E) and bile duct proliferation (Figure 2B) in the HRAS-HCC mouse model may obstruct the efflux of bile acids into the bile ducts, resulting in intrahepatic bile stasis and subsequent jaundice, possibly exacerbated by thrombus
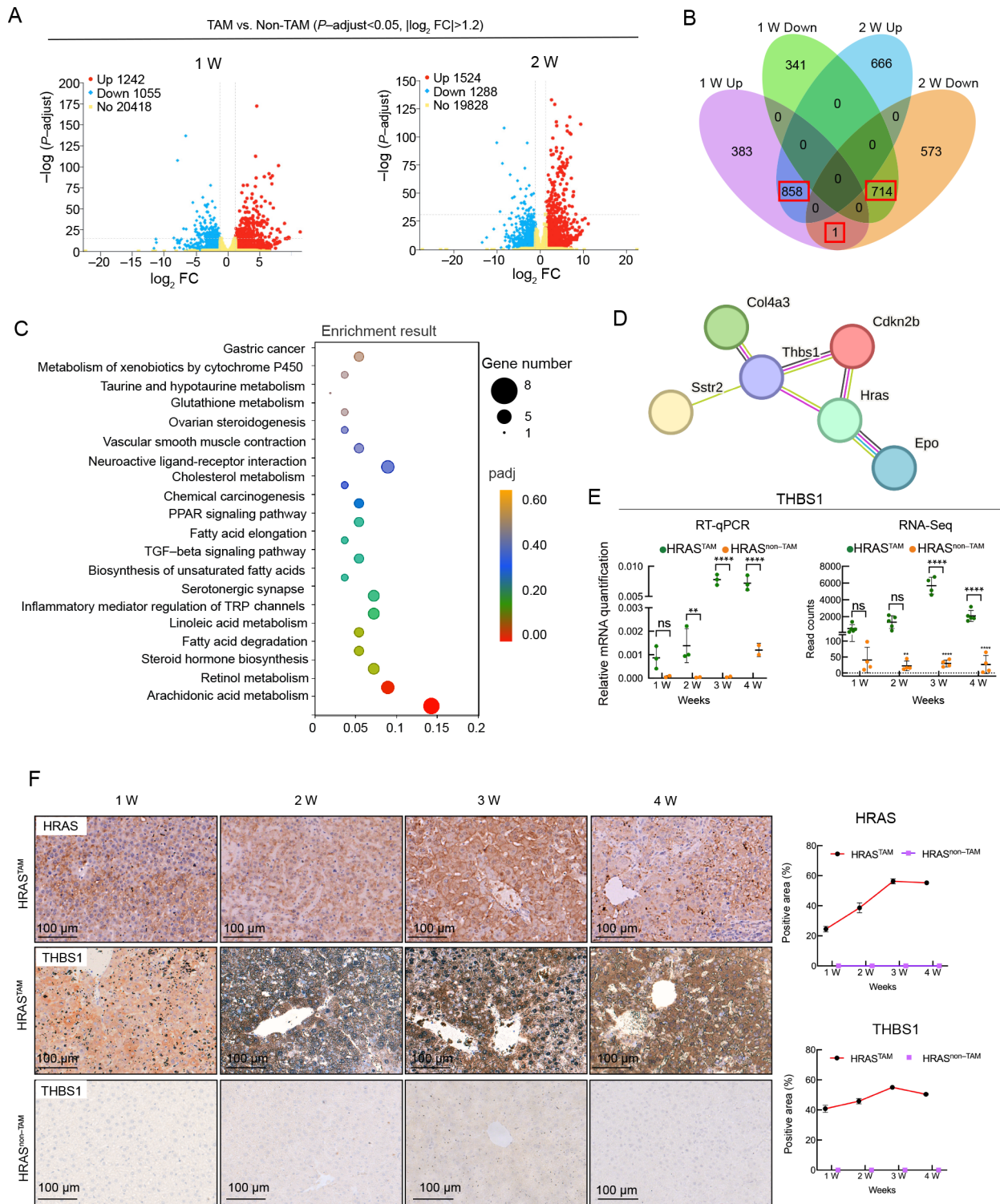
**Figure 6 Molecular interactions in HRAS-driven NASH-related HCC**

A: Volcano plots of DEGs in livers of HRAS[TAM]/HRAS[non-TAM] mice at weeks 1 and 2 (*P*-adjust<0.05, log$_2$|fold-change|>1.2). B: Venn diagram of DEGs from weeks 1 and 2. C: KEGG pathway enrichment analysis of top 100 up- and down-regulated DEGs from intersection genes at weeks 1 and 2. D: First HRAS-related functional module of PPI network in Supplementary Figure S5A. E: mRNA expression of *THBS1* in HRAS[TAM] and HRAS[non-TAM] mice by RT-qPCR (HRAS[TAM]: *n*=3; HRAS[non-TAM]: *n*=2; repeated three times) and RNA-seq (HRAS[TAM]: *n*=5; HRAS[non-TAM]: *n*=4). G: Immunohistochemical analysis of HRAS and THBS1 expression in liver tissue of HRAS[TAM] and HRAS[non-TAM] mice. Scale bar: 100 μm. Liver tissues were from the same mice in Figure 1J. ns: Not significant; [*]: *P*<0.05; [**]: *P*<0.01; [***]: *P*<0.001; [****]: *P*<0.0001.

formation within the bile ducts. Severe cases may involve malignant transformation accompanied by primary intrabiliary malignancies or metastatic cancer invading the bile ducts (Bittaye et al., 2023; Chen et al., 2021; Qin & Tang, 2003). In addition, hepatoma carcinoma cells leaving from cancer nests can migrate through the ECM, invade the vascular barrier, and colonize the portal vein, resulting in portal vein thrombosis, with some cancer cells disseminating to other organs, indicating metastasis (Zhou et al., 2023). Failure to recognize these phenomena often complicates preoperative diagnoses

and yields extremely poor prognoses.

Furthermore, the HRAS-HCC mouse model accurately mimicked the progression from NASH to HCC within a short duration. In humans, this transition arises from a complex interplay between environmental factors and genetic determinants (Farrel et al., 2019), exhibiting a variable, nonlinear pattern with distinct phases of progression. However, due to the slow progression of the disease in certain subpopulations, replicating this "jigsaw" pattern in animal models has proven challenging (Farrel et al., 2019; Ratziu, 2018). Remarkably, the HRAS-HCC mouse model exhibited a natural progression from NASH to minimal fibrosis, severe fibrosis, post-necrotic cirrhosis, and HCC, accompanied by detailed pathological descriptions (Figures 2–4). This comprehensive model offers a holistic view of the natural development of the disease, highlighting its potential utility in revealing the mechanisms underpinning HCC transition. Notably, although each stage displayed distinct features, signs of HCC were consistently visible, even in the early stages of NASH (Figure 2A). This phenomenon of coexisting NASH and HCC has also been observed in clinical patients (Kern et al., 2019).

The HRAS-HCC mouse model also served as a valuable preclinical tool for drug evaluation (Figure 5). Notably, sorafenib and anti-mouse PD-1 combination therapies (Tang et al., 2020; Yau et al., 2022) at the initial NASH stage prolonged the survival of HRAS-HCC mice, accompanied by reductions in the mRNA levels of *HRAS*, *TFRC*, *KRT18*, *FAH*, and *Ki67*, further confirming the applicability of our model (Figure 5). These findings suggest that immunotherapy may offer limited efficacy against non-viral HCC, particularly NASH-related HCC, consistent with clinical observations (Pfister et al., 2021). The inter-patient heterogeneity observed in HCC contributes to drug resistance (Mcgranahan & Swanton, 2017), while aberrant T cell activation induced by NASH can lead to tissue damage and impaired immune surveillance, representing another potential mechanism of drug resistance (Pfister et al., 2021). However, this high degree of heterogeneity also makes it challenging to identify useful single or combination biomarkers (Huang et al., 2020). Therefore, progress in this field relies on the availability of reliable preclinical models capable of investigating sensitivity and resistance to therapeutic agents during natural development of NASH-related HCC (Febbraio et al., 2019).

We hypothesized that the HRAS-THBS1-COL4A3 molecular axis, identified through RNA-seq and PPI analysis, potentially contributes to the progression of NASH-related HCC (Figure 6). In the HRAS-HCC mouse model, the overexpression of HRAS initiated a cascade of lipid metabolic signaling pathways related to NASH and carcinogenesis (Figure 6C). Of note, both THBS1 and COL4A3 were enriched in the PI3K-AKT signaling pathway and ECM-receptor interaction pathway. Our speculation is supported by several lines of evidence. Liver fibrosis and hepatic stellate cell (HSC) activation are modulated through mechanisms targeting inflammation, apoptosis, and ECM-receptor interactions, which are mediated by TGF-β signaling (Chen et al., 2023), with THBS1 enrichment observed in the TGF-β signaling pathway in the HRAS-HCC mouse model (Figure 6C; Supplementary Table S7). As a classical collagen protein, overexpression of COL4A3 has been extensively implicated in fibrosis (Unamuno et al., 2021) and NAFLD in zebrafish (Forn-

Cuní et al., 2015). Elevated THBS1 levels are positively correlated with TG and CHO levels (Gao et al., 2023), as well as liver steatosis grades (Bai et al., 2020). Additionally, increased THBS1 expression has been linked to the activation of epithelial mesenchymal transition (Murphy-Ullrich & Suto, 2018), collagen fibril formation (Rosini et al., 2018), fibroblast migration and activation (Lu et al., 2011), and invasion and migration of gastric cancer cells via the PI3K/AKT/mTOR pathway (Lin et al., 2012). The positive correlation detected between high levels of HRAS, THBS1, and COL4A3 across NASH stages, including fibrosis and HCC (Figures 4, 6), indirectly supports the HRAS-THBS1-COL4A3 molecular axis hypothesis. Overall, the function of the HRAS-THBS1-COL4A3 axis in the occurrence and stage transition of NASH-HCC may hold significant value, but further experiments, such as gene deficiency studies targeting *THBS1* or *COL4A3*, are urgently needed.

Overexpression of the wild-type *HRAS* gene may serve as a prominent causative factor for NASH-related HCC, despite *HRAS* gene mutations being considered the primary mechanism of carcinogenesis (Li et al., 2018). Notably, in the HRAS-HCC model, NASH-related HCC occurred under overexpression of the wild-type *HRAS* gene (Figure 1F–J; Supplementary Figure S1E–J), a phenomenon supported by clinical data from the TCGA, GEO and KM-Plotter databases (Figure 1A–D; Supplementary Figure S1A–D). Recent studies have suggested that m[6]A modification can promote wild-type RAS protein overexpression, contributing to tumorigenesis (Alejandro et al., 2022; Pan et al., 2023). However, the precise role of the *HRAS* gene in HCC remains elusive (Pan et al., 2023), necessitating further study. In other cancer types, existing evidence has indicated that normal *HRAS* gene overexpression can drive gastric carcinoma and non-small-cell lung cancer and may also be correlated with breast cancer (Pązik et al., 2021; Wu et al., 2016).

While several novel findings were presented in the HRAS-HCC mouse model, further clarification is required regarding certain characteristics. The decreased serum ALT level in the HRAS-HCC mouse model contradicts previous research (Supplementary Figure S2). Although elevated serum ALT levels are commonly considered diagnostic indicators for NAFLD, some NAFLD patients may still exhibit normal levels even in advanced stages of liver fibrosis (Fracanzani et al., 2008; Mofrad et al., 2003; Verma et al., 2013). Additionally, the precise role of diet and lifestyle in the progression of HCC remains inadequately elucidated. While western diet and lifestyle are often regarded as key triggers in the progression of NASH to HCC, the impact of liver injury severity and clinical outcomes in lean individuals with NAFLD remains unclear, with limited studies exploring these aspects in the general population (Nabi et al., 2023). Consequently, investigating other pathogenic factors associated with HCC using the HRAS-HCC model may be a valuable approach.

In conclusion, we successfully established a rapid-onset, clinically faithful model of HCC. We delineated the complex and comprehensive tumor progression, capturing the stages from NASH, fibrosis, cirrhosis, and HCC in a single mouse model. Thus, the HRAS-HCC model holds immense potential for elucidating the intricacies of tumorigenesis, unveiling the mechanism of transition, devising novel therapeutic strategies, and unraveling the previously unknown role of the *HRAS* gene in driving carcinogenesis.

## REFERENCES

Alejandro MH, Clara LO, Claudia C, et al. 2022. Overexpression of wild type RRAS2, without oncogenic mutations, drives chronic lymphocytic leukemia. Molecular Cancer, 21(1): 35.

Alqudah M, Taben MH, Czubryt P. 2020. Targeting the renin-angiotensin-aldosterone system in fibrosis. Matrix Biology, 91-92: 92–108.

Anstee QA, Helen Lr, Elena K, et al. 2019. From NASH to HCC: current concepts and future challenges. Nature Reviews Gastroenterol & Hepatology, 16(7): 411–428.

Atanasova SV, Rebecca JR, Timothy GW, et al. 2019. Thrombospondin-1 is a major activator of TGF-β signaling in recessive dystrophic epidermolysis bullosa fibroblasts. Journal of Investigative Dermatology, 139(7): 1497–1505.

Bai JY, Xia MF, Xue YQ, et al. 2020. Thrombospondin 1 improves hepatic steatosis in diet-induced insulin-resistant mice and is associated with hepatic fat content in humans. EBioMedicine, 57: 102849.

Behera JR, Pattanaik S, Jain M. 2020. An infant with milky serum and a rare mutation. Indian Pediatr, 57(1): 73–74.

Bittaye SO, Abubacarr K, Momodou Ait, et al. 2023. Clinical manifestation, staging and prognosis of hepatocellular carcinoma in Gambian patients. BMC Gastroenterology, 23(1): 321.

Blackburn PR, Raymond DH, Rebecca AN, et al. 2016. Silent tyrosinemia type I without elevated tyrosine or succinylacetone associated with liver cirrhosis and hepatocellular carcinoma. Human Mutation, 37(10): 1097–1105.

Chang Y, Jeong SW, Young JJ, Kim JY. 2020. Recent updates of transarterial chemoembolilzation in hepatocellular carcinoma. International Journal of Molecular Sciences, 21(21): 8165.

Chaurasiya OS, Kumar L, Sethi RS. 2013. An infant with milky blood : an unusual but treatable case of familial hyperlipidemia. *Indian Journal of Clinical Biochemistry*, **28**(2): 206–209.

Chen C, Chen J, Wang Y, et al. 2023. Ganoderma lucidum polysaccharide inhibits HSC activation and liver fibrosis via targeting inflammation, apoptosis, cell cycle, and ECM-receptor interaction mediated by TGF-beta/Smad signaling. Phytomedicine, 110: 154626.

Chen PD, Chen Lj, Chang Yj, Yj C. 2021. Long-term survival of combined hepatocellular-cholangiocarcinoma: a nationwide study. Oncologist, 26(10): e1774–e1785.

Chinese Society of Hepatology CMA, Chinese Society of Gastroenterology CMA, Chinese Society of Infectious Diseases CMA. 2020. Consensus on the diagnosis and treatment of hepatic fibrosis (2019). Journal of Digestive Diseases, 21(3): 127–138.

Chuah S, Lee J, Song Y, et al. 2022. Uncoupling immune trajectories of response and adverse events from anti-PD-1 immunotherapy in hepatocellular carcinoma. Journal of Hepatology, 77(3): 683–694.

Connor F, Rayner TF, Aitken SJ, et al. 2018. Mutational landscape of a chemically-induced mouse model of liver cancer. Journal of Hepatology, 69(4): 840–850.

Daniel C, Wiede J, Krutzsch HC, et al. 2004. Thrombospondin-1 is a major activator of TGF-beta in fibrotic renal disease in the rat in vivo. Kidney International, 65(2): 459–468.

De La Rosa L, Carmen G, Carmen V, et al. 2021. STARD1 promotes NASH-driven HCC by sustaining the generation of bile acids through the alternative mitochondrial pathway. Journal of Hepatology, 74(6): 1429–1441.

De La Vega MR. 2023. A holistic view of cancer. Cancer Cell, 41(3): 373.

De Martin E, Michot JM, Olivier R, et al. 2020. Liver toxicity as a limiting factor to the increasing use of immune checkpoint inhibitors. JHEP Reports, 2(6): 100170–100183.

Dildar S and Shamsi TS. 2020. Case report of one month and 15 days old baby with type V hyperlipoproteinemia (HLP). BMC Endocrine Disorders, 20(1): 22–27.

Donne R and Lujambio A. 2023. The liver cancer immune microenvironment: Therapeutic implications for hepatocellular carcinoma. Hepatology, 77(5): 1773–1796.

Dowman JK, Hopkins LJ, Reynolds GM, et al. 2014. Development of hepatocellular carcinoma in a murine model of nonalcoholic steatohepatitis induced by use of a high-fat/fructose diet and sedentary lifestyle. American Journal of Pathology, 184(5): 1550–1561.

Eslam M, Sanyal AJ, George J. 2020. MAFLD: a consensus-driven proposed nomenclature for metabolic associated fatty liver disease. Gastroenterology, 158(7): 1999–2014.

Farrel G, Jörn MS, Isabelle L, et al. 2019. Mouse models of nonalcoholic steatohepatitis: toward optimization of their relevance to human nonalcoholic steatohepatitis. Hepatology, 69(5): 2241–2257.

Febbraio MA, Reibe S, Shalapour S, et al. 2019. Preclinical models for studying NASH-driven HCC: how useful are they. Cell Metabolism, 29(1): 8.

Feil S, Valtcheva N, Feil R. 2009. Inducible Cre mice. Methods in Molecular Biology, 530: 343–363.

Foerster F, Gairing SJ, Muller L, Galle PR. 2022. NAFLD-driven HCC: safety and efficacy of current and emerging treatment options. Journal of Hepatology, 76(2): 446–457.

Forn-Cuní G, Varela M, Fernandez-Rodriguez CM, et al. 2015. Liver immune responses to inflammatory stimuli in a diet-induced obesity model of zebrafish. Journal of Endocrinological Investigation, 224(2): 159–170.

Fracanzani AL, Valenti L, Bugianesi E, et al. 2008. Risk of severe liver disease in nonalcoholic fatty liver disease with normal aminotransferase levels: a role for insulin resistance and diabetes. Hepatology, 48(3): 792–798.

Fujii M, Shibazaki Y, Wakamatsu K, et al. 2013. A murine model for non-alcoholic steatohepatitis showing evidence of association between diabetes and hepatocellular carcinoma. Medical Molecular Morphology, 46(3): 141–152.

Fujiwara N, Nakagawa H, Enooku K, et al. 2018. CPT2 downregulation adapts HCC to lipid-rich environment and promotes carcinogenesis via acylcarnitine accumulation in obesity. Gut, 67(8): 1493–1504.

Gandhi CR, Chaillet JR, Nalesnik MA, et al. 2015. Liver-specific deletion of augmenter of liver regeneration accelerates development of steatohepatitis and hepatocellular carcinoma in mice. Gastroenterology, 148(2): 379–391.

Gao H, Li Y, Jin Y, et al. 2023. Electroacupuncture activates angiogenesis by regulating the PI3K/Pten/Thbs1 signaling pathway to promote the browning of adipose tissue in HFD-induced obese mice. Biomedicine& Pharmacotherapy, 166: 115386.

Garcia-Tsao G, Lim JK, Members of Veterans Affairs Hepatitis CRCP. 2009. Management and treatment of patients with cirrhosis and portal hypertension: recommendations from the department of veterans affairs hepatitis C resource center program and the national hepatitis C program. American Journal of Gastroenterology, 104(7): 1802–1829.

Guo P, Zuo J, Huang KK, et al. 2023. Cell atlas of CCl4-induced progressive liver fibrosis reveals stage-specific responses. Zoological Research, 44(3): 451–466.

Hou W, Liu J, Chen P, et al. 2014. Mutation analysis of key genes in RAS/RAF and PI3K/PTEN pathways in Chinese patients with hepatocellular carcinoma. Oncology Letters, 8(3): 1249–1254.

Huang A, Yang XR, Chung WY, et al. 2020. Targeted therapy for hepatocellular carcinoma. Signal Transduction and Targeted Therapy, 5(1): 146.

Jeng LB, Chan WL, Teng CF. 2023. Prognostic significance of serum albumin level and Albumin-based mono- and combination biomarkers in patients with hepatocellular carcinoma. Cancers (Basel), 15(4): 1005–1028.

Karlsson K, Przybilla MJ, Kotler E, et al. 2023. Deterministic evolution and stringent selection during preneoplasia. Nature, 618(7964): 383–393.

Kawai D, Takaki A, Nakatsuka A, et al. 2012. Hydrogen-rich water prevents progression of nonalcoholic steatohepatitis and accompanying hepatocarcinogenesis in mice. Hepatology, 56(3): 912–921.

Kern B, Benedikt F, Osef F, et al. 2019. High incidence of hepatocellular carcinoma and postoperative complications in patients with nonalcoholic steatohepatitis as a primary indication for deceased liver transplantation. European Journal of Gastroenterology & Hepatology, 31(2): 205–210.

Kim H, Choi J, Yu DY, Choi HJ. 2021. Expression of organic anion transporting polypeptides in an H-Ras 12V transgenic mouse model of spontaneous hepatocellular carcinoma. Yonsei Medical Journal, 62(7): 622–630.

Krizhanovsky V, Yon M, Dickins RA, et al. 2008. Senescence of activated stellate cells limits liver fibrosis. Cell, 134(4): 657–667.

Li S, Balmain A, Counter CM. 2018. A model for RAS mutation patterns in cancers: finding the sweet spot. Nat Rev Cancer, 18(12): 767–777.

Lin XD, Chen SQ, Qi YL, et al. 2012. Overexpression of thrombospondin-1 in stromal myofibroblasts is associated with tumor growth and nodal metastasis in gastric carcinoma. Journal Of Surgical Oncology, 106(1): 94–100.

Liu J, Ayada I, Zhang X, et al. 2022. Estimating global prevalence of metabolic dysfunction-associated fatty liver disease in overweight or obese adults. Clinical Gastroenterology and Hepatology, 20(3): e573–e582.

Liu S, Wu X, Zhou S, et al. 2018. Generation of human HRAS geneconditional knockin mouse using the Cre-LoxP strategy. Laboratory animal science (Chinese), 35(4): 21–28.

Lizen B, Claus M, Jeannotte L, et al. 2015. Perinatal induction of Cre recombination with tamoxifen. Transgenic Research, 24(6): 1065–1077.

Lu A, Miao M, Schoeb TR, et al. 2011. Blockade of TSP1-dependent TGF-beta activity reduces renal injury and proteinuria in a murine model of diabetic nephropathy. American Journal of Pathology, 178(6): 2573–2586.

Mcglynn KA, Petrick JL, El-Serag HB. 2021. Epidemiology of hepatocellular carcinoma. *Hepatology*, **73 Suppl 1**(Suppl 1): 4-13.

Mcgranahan N and Swanton C. 2017. Clonal heterogeneity and tumor evolution: past, present, and the future. Cell, 168(4): 613–628.

Mofrad P, Contos MJ, Haque M, et al. 2003. Clinical and histologic spectrum of nonalcoholic fatty liver disease associated with normal ALT values. Hepatology, 37(6): 1286–1292.

Moore RA, Scott CR, Frank M, Shiva M. 2022. RAS-targeted therapies: is the undruggable drugged?. Nature Reviews Drug Discovery, 19(8): 533–552.

Mu XM, Wang W, Jiang YY, Feng J. 2020. Patterns of Comorbidity in Hepatocellular Carcinoma: A Network Perspective. International Journal of Environmental Research and Public Health, 17(9): 3108.

Mudumbi SK, Bourgeois CE, Hoppman NA, et al. 2018. Palliative care and hospice interventions in decompensated cirrhosis and hepatocellular carcinoma: a rapid review of literature. Journal of Palliative Medicine, 21(8): 1177–1184.

Murphy-Ullrich JE and Suto M. 2018. Thrombospondin-1 regulation of latent TGF-beta activation: A therapeutic target for fibrotic disease. Matrix Biology, 68-69: 28–43.

Nabi O, Nathanaël L, Jerome B, et al. 2023. Lean individuals with NAFLD have more severe liver disease and poorer clinical outcomes (NASH-CO Study). Hepatology, 78(1): 272–283.

Newell P, Toffanin S, Villanueva A, et al. 2009. Ras pathway activation in hepatocellular carcinoma and anti-tumoral effect of combined sorafenib and rapamycin in vivo. Journal of Hepatology, 51(4): 725–733.

Orci LA, Sanduzzi-Zamparelli M, Caballol B, et al. 2022. Incidence of hepatocellular carcinoma in patients with nonalcoholic fatty liver disease: a systematic review, meta-analysis, and meta-regression. *Clinical Gastroenterology and Hepatology*, **20**(2): 283-292. e210.

Pan Y, Gu Y, Liu T, et al. 2023. Epitranscriptic regulation of HRAS by N(6)-methyladenosine drives tumor progression. Proceedings of the National Academy of Sciences, 120(14): e2302291120.

Pązik M, Michalska K, Zebrowska-Nawrocka M, et al. 2021. Clinical significance of HRAS and KRAS genes expression in patients with non-small-cell lung cancer - preliminary findings. BMC Cancer, 21(1): 130.

Pfister DandNunez NGandPinyol R, et al. 2021. NASH limits anti-tumour surveillance in immunotherapy-treated HCC. Nature, 592(7854): 450–456.

Poujois A and Woiman F. 2018. Wilson's disease: A 2017 update. Clinics and Research in Hepatology and Gastroenterology, 42(6): 512–520.

Powell EE, Cooksley WG, Hanson R, et al. 1990. The natural history of nonalcoholic steatohepatitis: a follow-up study of forty-two patients for up to 21 years. Hepatology, 11(1): 74–80.

Powell EE, Wong VW, Rinella M. 2021. Non-alcoholic fatty liver disease. Lancet, 397(10290): 2212–2224.

Premkumar M and Anand CA. 2021. Lean fatty liver disease: through thick and thin. *Journal of Clinical and Experimental Hematopathology* **11**(5): 523–527.

Qin LX and Tang ZY. 2003. Hepatocellular carcinoma with obstructive jaundice: diagnosis, treatment and prognosis. World Journal of Gastroenterology, 9(3): 385–391.

Rahme JG, Nauman MJ, Kaitlyn LP, et al. 2023. Modeling epigenetic lesions that cause gliomas. *Cell*, **186**(17): 3674-3685. e3614.

Ratziu V. 2018. A critical review of endpoints for non-cirrhotic NASH therapeutic trials. Journal of Hepatology, 68(2): 353–361.

Reinert BR, Jeannelle K, Amanda AM, et al. 2012. Tamoxifen-induced Cre-loxP recombination is prolonged in pancreatic islets of adult mice. PloS One, 7(3): e33529.

Rittié L. 2017. Method for picrosirius red-polarization detection of collagen fibers in tissue sections. Methods in Molecular Biology, 1627: 385–397.

Rosini S, Pugh N, Bonna AM, et al. 2018. Thrombospondin-1 promotes matrix homeostasis by interacting with collagen and lysyl oxidase precursors and collagen cross-linking sites. *Science Signaling*, **11**(532).

Schott MBS, Shaun GW, Ryan JS, et al. 2019. Lipid droplet size directs lipolysis and lipophagy catabolism in hepatocytes. Journal of Cell Biology, 218(10): 3320–3335.

Schubbert S, Shannon K, Bollag G. 2007. Hyperactive Ras in developmental disorders and cancer. Nature Reviews Cancer, 7(4): 295–308.

Sheka AC, Adeyi O, Thompson J, et al. 2020. Nonalcoholic steatohepatitis: a review. The Journal of the American Medical Association, 323(12): 1175–1183.

Shi J, Liu J, Tu X, et al. 2022. Single-cell immune signature for detecting early-stage HCC and early assessing anti-PD-1 immunotherapy efficacy. Journal for ImmunoTherapy of Cancer, 10(1): e003133.

Su WH, Qiu T, Zhang M, et al. 2022. Systems biomarker characteristics of circulating alkaline phosphatase activities for 48 types of human diseases. Current Medical Research and Opinion, 38(2): 201–209.

Suzuki S, Divya V, Hiroaki K, et al. 2022. GLS2 is a tumor suppressor and a regulator of ferroptosis in hepatocellular carcinoma. Cancer Research, 82(18): 3209–3222.

Takeuchi M, Shichinohe T, Senmaru N, et al. 2000. The dominant negative H-ras mutant, N116Y, suppresses growth of metastatic human pancreatic cancer cells in the liver of nude mice. Gene Therapy, 7(6): 518–526.

Tang W, Chen Z, Zhang W, et al. 2020. The mechanisms of sorafenib resistance in hepatocellular carcinoma: theoretical basis and therapeutic aspects. Signal Transduction and Targeted Therapy, 5(1): 87.

Tang Z, Qin L, Wang X, et al. 1998. Alterations of oncogenes, tumor suppressor genes and growth factors in hepatocellular carcinoma: with relation to tumor size and invasiveness. Chinese Medical Journal 111(4): 313–318.

Thaler H. 1962. The fatty liver and its pathogenetic relation to liver cirrhosis. Virchows Archiv für Pathologische Anatomie und Physiologie und für Klinische Medizin, 335: 180–210.

Tsuchida T, Lee YA, Fujiwara N, et al. 2018. A simple diet- and chemical-induced murine NASH model with rapid progression of steatohepatitis, fibrosis and liver cancer. Journal of Hepatology, 69(2): 385–395.

Unamuno X, Gomez-Ambrosi J, Ramirez B, et al. 2021. NLRP3 inflammasome blockade reduces adipose tissue inflammation and extracellular matrix remodeling. Cellular & Molecular Immunology, 18(4): 1045–1057.

Verma S, Jensen D, Hart J, Mohanty SR. 2013. Predictive value of ALT levels for non-alcoholic steatohepatitis (NASH) and advanced fibrosis in non-alcoholic fatty liver disease (NAFLD). Liver International, 33(9): 1398–1405.

Wang H, Fu Y, Da BB, Xiong G. 2022. Single-cell sequencing identifies the heterogeneity of CD8+ T cells and novel biomarker genes in hepatocellular carcinoma. Journal of Healthcare Engineering, 12: 2022: 8256314.

Wang LP, Luo Q, Zeng Sj, et al. 2021. Disordered farnesoid X receptor signaling is associated with liver carcinogenesis in Abcb11-deficient mice. Journal of Pathology, 255(4): 412–424.

Wu J. 2016. Utilization of animal models to investigate nonalcoholic steatohepatitis-associated hepatocellular carcinoma. Oncotarget, 7(27): 42762–42776.

Wu XY, Liu WT, Zhen FW, et al. 2016. Identification of HRAS as cancer-promoting gene in gastric carcinoma cell aggressiveness. American Journal of Cancer Research, 6(9): 1935–1948.

Yahoo N, Dudek M, Knolle P, Heikenwalder M. 2023. Role of immune responses in the development of NAFLD-associated liver cancer and prospects for therapeutic modulation. Journal of Hepatology, 79(2): 538–551.

Yang YP, Guan XQ, Qi MM, Zhu LR. 2012. Effects of resistin on hepatic fibrosis: possible mechanisms in non-alcoholic fatty liver disease in in vitro and in vivo. Zoological Research, 33(4): 367–372.

Yau T, Park JW, Finn RS, et al. 2022. Nivolumab versus sorafenib in advanced hepatocellular carcinoma (CheckMate 459): a randomised, multicentre, open-label, phase 3 trial. Lancet Oncology, 23(1): 77–90.

Young RH. 2018. Ovarian sex cord-stromal tumours and their mimics. Pathology, 50(1): 5–15.

Younossi ZM, Anstee QM, Marietti M, et al. 2018a. Global burden of NAFLD and NASH: trends, predictions, risk factors and prevention. Nature Reviews Gastroenterology & Hepatology, 15(1): 11–20.

Younossi ZM, Loomba R, Anstee QM, et al. 2018b. Diagnostic modalities for nonalcoholic fatty liver disease, nonalcoholic steatohepatitis, and associated fibrosis. Hepatology, 68(1): 349–360.

Zhang GB, Song YN, Chen QL, et al. 2015. Actions of Huangqi decoction against rat liver fibrosis: a gene expression profiling analysis. Chinese Medicine, 10: 39.

Zhou XH, Li JR, Zheng TH, et al. 2023. Portal vein tumor thrombosis in hepatocellular carcinoma: molecular mechanism and therapy. Clinical & Experimental Metastasis, 40(1): 5–32.

Zhu YL, Meng LL, Ma JH, et al. 2024. Loss of LBP triggers lipid metabolic disorder through H3K27 acetylation-mediated C/EBPβ-SCD activation in non-alcoholic fatty liver disease. Zoological Research, 45(1): 79–94.